Supporting Information

Trebbin et al. 10.1073/pnas.1219340110

SI Text

Fabrication of Kapton–Polydimethylsiloxane–Kapton Microfluidic Devices. The fabrication of Kapton–polydimethylsiloxane (PDMS)–Kapton microfluidic devices is illustrated in Fig. S1. A negative photoresist (SU-8 50; Microchem Co.) is spin-coated onto a silicon wafer. A mask aligner (Süss Mikro Tec) is used to impart the microchannel structure into the photoresist. We optimize the master device fabrication to obtain microchannels with a very uniform height of 100 μm. Although PDMS is widely applied to replicate the microchannel master device using soft lithography, PDMS scatters and absorbs X-rays. To fabricate X-ray–compatible microfluidic devices involving PDMS, we modified the conventional fabrication procedure, based on the work of Evans et al. (1) and Dootz et al. (2). After pouring PDMS prepolymer (Sylgard 184; Dow Corning) on the master device, excess prepolymer is removed from the master device with a razor blade. The remaining PDMS is cured, and a small piece of self-adhesive polyimide tape (Kapton; DuPont) is used to cover the area of interest of the microchannel network, including the curved and tapered microchannel sections. A second layer of PDMS is cured onto the previous layers. The PDMS replica is removed from the master device, and inlet ports are punched into the polymer using a biopsy punch needle (0.75-mm Uni-Core; Harris). The bottom of the device is sealed with Kapton tape, and a window is cut into the top PDMS layer. Thus, the microchannels in the area of interest are solely sealed with X-ray transparent Kapton tape.

Computational Fluid Dynamics Simulations. The non-Newtonian flow behavior of the aqueous solution of block copolymer wormlike micelles is characterized by a shear rate-dependent viscosity η. The experimental data on η are obtained by rheometry using a Gemini 200 (Bohlin), and they are shown in Fig. S2. The data in Fig. S2 are fitted by the shear rate-dependent viscosity according to the Cross (3) equation (4):

$$\eta = \eta_\infty + \frac{\eta_0 - \eta_\infty}{1 + \left(\tau_c \dot{\gamma}\right)^n}.$$

Herein, η_0 describes the zero-shear viscosity, η_∞ the high-shear viscosity, τ_c the internal relaxation time, and n the power-law exponent characterizing the shear thinning between η_0 and η_∞.

The dynamics of the velocity field $\vec{v}$ of the incompressible non-Newtonian fluid are described by the Navier–Stokes equation with the shear rate-dependent viscosityη (5):

$$\nabla \cdot \vec{v} = 0$$

$$\rho \partial_t \vec{v} + \rho\left(\vec{v} \cdot \nabla\right)\vec{v} = \nabla \cdot \left[-p\mathbf{I} + \eta\left(\nabla\vec{v} + \nabla\vec{v}^T\right)\right],$$

with the constant density of the fluid ρ and the unity matrix $\mathbf{I}$.

The equation is solved with COMSOL Multiphysics v4.2a software (6). In a first step, the CAD-designed microchannel geometry is imported to COMSOL and finite elements are generated based on this geometry. Thereafter, boundary conditions are assigned to the elements to match the experiment under stationary conditions. The model is solved for 1,412,784 finite elements and 1,072,212 df. The average element quality of the mesh is 0.9889 on a scale from 0 to 1, where 1 is the highest quality and the minimal element quality is 0.6923. All relevant parameters used in the simulations are summarized in Table S1.

Calculated Velocity Field for Water. The calculated velocity field for a shear-thinning fluid with the shear-dependent viscosity of wormlike micelles has been discussed in the main text. Here, we present the same calculations for water as a Newtonian fluid. This provides insight to what extent the shear thinning widens the range of extensional flow in the expansion zone after a narrow channel section. We calculated the velocity field for water under the same experimental conditions as for wormlike micelles. The results are shown in Fig. S3, which is organized similar to Fig. 5 for comparison.

For water, the expected parabolic flow profile $v_x(y)$ is observed, as shown in Fig. S3 (*B* and *C*), with the corresponding linear increase of the shear rate $\dot{\gamma}(y)$ toward the channel walls (Fig. S3*D*). The extensional rate $\dot{\varepsilon} = -\nabla_y v_y$ smoothly decreases from small positive values in the central part of the channel to small negative values close to the channel walls. For comparison with the color maps in the main text (Figs. 4*F* and 5*E*), we visualize zones with high extensional rates $\dot{\varepsilon}/|\dot{\gamma}| > 0.14$ in orange and zones with high shear rates $\dot{\varepsilon}/|\dot{\gamma}| < 0.14$ in blue, using the same threshold value of $\dot{\varepsilon}/|\dot{\gamma}| = 0.14$ as shown in Fig. S3*E*. In the case of a Newtonian fluid, such as water, the high extensional rate zone (orange, Fig. S3*E*) is limited to a small region in the central part of the channel. Thus, a high perpendicular extensional rate zone is also present in Newtonian fluids but becomes larger and more pronounced in non-Newtonian, shear-thinning fluids.

Microparticle Image Velocimetry and Measured Velocity Fields of Water. To obtain the velocity flow profile $\vec{v}(x,y)$experimentally, we used microparticle image velocimetry (μPIV). The setup involves an Olympus IX71 inverse microscope, a phantom v9.1 high-speed camera (Vision Research), and a highly intense, focused light source. This setup allows exposures down to 2 μs and frame rates up to 150,000 s^{-1}. The narrow depth of focus of the setup enables precise vertical position control within the microchannel. The obtained high-speed image sequence is autocorrelated and analyzed using the open-source software package JPIV (7). Measurements were made in pure water and in aqueous solutions of cylindrical micelles at 25% wt/wt. Each solution contained 2% wt/wt of monodisperse polystyrene tracer particles (3.3-μm diameter), which were coated with polyacrylic acid to avoid wall adhesion. Each solution is pumped through a 250-μm channel with a height of 110 μm at a flow rate of 32.7 $\mu L \cdot h^{-1}$. The channel's tapering had a width ratio of 5:1 and a length of 500 μm.

The results for the shear-thinning wormlike micelle solutions are discussed in the main text. Here, we present the comparison with the flow behavior of pure water, a Newtonian fluid. The analysis shows that the key features of the velocity fields obtained from computational fluid dynamics (CFD) simulations agree well with the experimentally determined velocity fields. The expected nearly parabolic flow profile $v_x(y)$ is observed in all channel sections, which is shown in Fig. S4 *B* and *C*. As shown in Fig. S4*D*, in the expansion zone, the extensional rate $\dot{\varepsilon}(y)$ smoothly decreases from small positive values in the central part of the channel to small negative values close to the channel walls. For comparison with the color maps in the main text (Figs. 4*F* and 5*E*), we visualize zones with high extensional rates $\dot{\varepsilon}/|\dot{\gamma}| > 0.14$ in orange and zones with high shear rates $\dot{\varepsilon}/|\dot{\gamma}| < 0.14$ in blue, using the same threshold value of $\dot{\varepsilon}/|\dot{\gamma}| = 0.14$ as shown in Fig. S4*E*. Similar to the CFD simulations, in case of a Newtonian fluid, such as water, the high extensional rate zone (orange, Fig. S4*D*) is limited to a smaller region in the central part of the channel.

Microchannels with Double Tapering. The flow behavior of wormlike micelles in consecutive taperings is studied in a 250-μm channel with a 5:1 tapering ratio. In the expansion zone of the first tapering, the micelles (30% wt/wt) orient perpendicular to the flow direction, which is indicated by the orange birefringence interference colors in Fig. S5. This orientation is switched back to the parallel alignment when entering the compression zone of the subsequent tapering, as indicated by the blue birefringence interference colors in Fig. S5.

Detailed Small-Angle X-Ray Scattering Pattern Analysis. Fig. S6 shows typical scattering patterns measured in the contraction zone (Fig. S6*A*), in the beginning of the expansion zone (Fig. S6*B*), and in the central part of the expansion zone (Fig. S6*C*). The azimuthal peak positions change from the meridian (Fig. S6*A*) via a Debye–Scherrer ring (Fig. S6*B*) to the equatorial position, indicating a change of the orientational distribution of the micelles from an alignment parallel to the flow direction via an isotropic orientational to an orientation perpendicular to the flow direction. The isotropic orientation is likely caused by the limited spatial resolution determined by the diameter of the X-ray beam, which probes different fluid volumes with different micellar orientations.

The radial peak positions do not change. A detailed analysis of the scattering patterns is performed via simulations, which are shown in Fig. S6. The simulations are performed assuming a hexagonal packing of homogeneous cylinders exhibiting an Onsager-type orientational distribution. Details of the simulations are given by Förster et al. (8). The structural parameters used for the simulations are summarized in Table S2.

Influence of Flow Rates. The influence of different flow rates on the extent of the perpendicular micelle alignment is studied by polarization microscopy. The results show that the perpendicular-oriented zone increases in size with decreasing flow rates. Additionally performed CFD simulations show the same trend and are in good agreement with experimental results, as shown in Fig. S7. Each experiment is performed in a tapered microchannel with a channel width of 500 μm and channel height of 100 μm. The tapering length is 2,500 μm, with a tapering ratio of 7.5:1 (67 μm). The 30% wt/wt solution of polyethylenebutylene-*b*-ethylene oxide cylindrical micelles is flowing at a rate of 200 or 2,000 μL/h. The CFD simulation was performed under the same conditions as the simulations described above.

1. Evans HM, Dootz R, Köster S, Struth B, Pfohl T (2007) X-ray microdiffraction on flow-controlled biomolecular assemblies. *Bulletin of the Polish Academy of Sciences, Technical Sciences* 55(2):217–227.
2. Dootz R, Evans H, Köster S, Pfohl T (2007) Rapid prototyping of X-ray microdiffraction compatible continuous microflow foils. *Small* 3(1):96–100.
3. Cross M (1965) Rheology of non-Newtonian fluids: A new flow equation for pseudoplastic systems. *J Colloid Sci* 20(5):417–437.
4. Förster S, Konrad M, Lindner P (2005) Shear thinning and orientational ordering of wormlike micelles. *Phys Rev Lett* 94(1):017803.
5. Bird BB, Armstrong RC, Hassager C (1987) *Dynamics of Polymeric Liquids* (Wiley, New York).
6. (2011) *User's Guide for COMSOL Multiphysics v4.2a* (COMSOL AB), pp 612–627.
7. JPIV v1.0: Open source software package for particle image velocimetry. Available at www.jpiv.vennemann-online.de. Accessed October 2, 2012.
8. Förster S, Apostol L, Bras W (2010) Scatter: A software for the analysis of nano- and mesoscale small-angle scattering. *J Appl Cryst* 43:639–646.

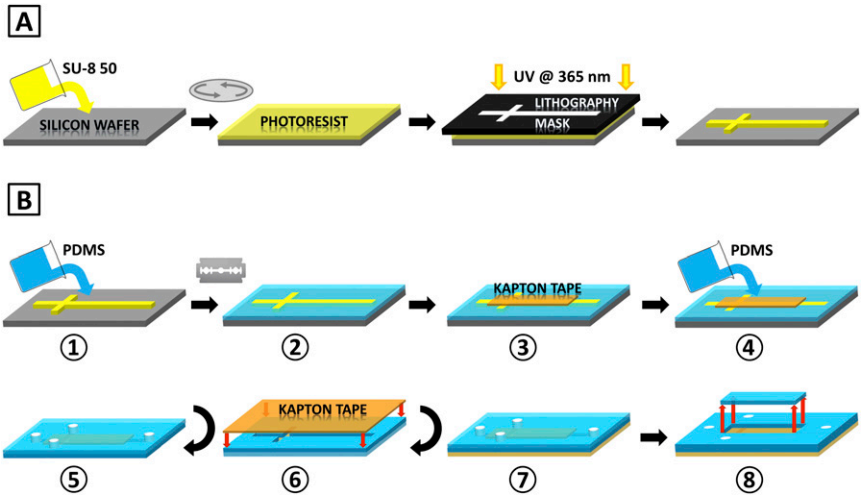

Fig. S1. Fabrication of microfluidic devices with X-ray analysis capability based on PDMS. (*A*) Master device fabrication using photolithography. (SU-8 50 photoresist) (*B*) Fabrication of X-ray transparent microfluidic Kapton–PDMS–Kapton sandwich devices. PDMS is poured on a master device (1), and excess PDMS is cut off the microchannel structure (2). Self-adhesive Kapton tape is used to seal the area of interest (3), and a second layer of PDMS is grafted on top (4). (5) PDMS replica is peeled off the master device, and inlet ports for fluids are added. The bottom is sealed with Kapton tape (6), before a window is cut into the top PDMS layer with similar dimensions as the Kapton window in 3 (7 and 8).

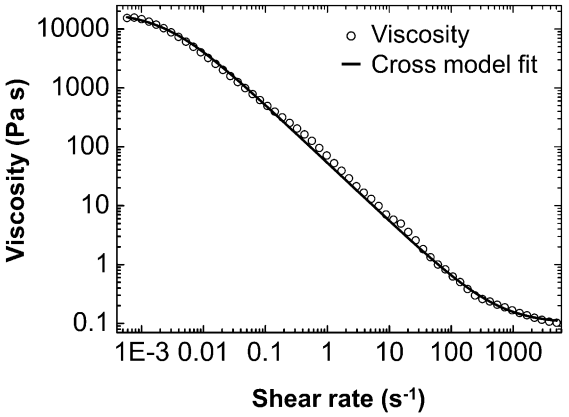

Fig. S2. Experimental rheological data. Viscosity (η) as a function of the shear rate ($\dot{\gamma}$) is described by the Cross equation (3).

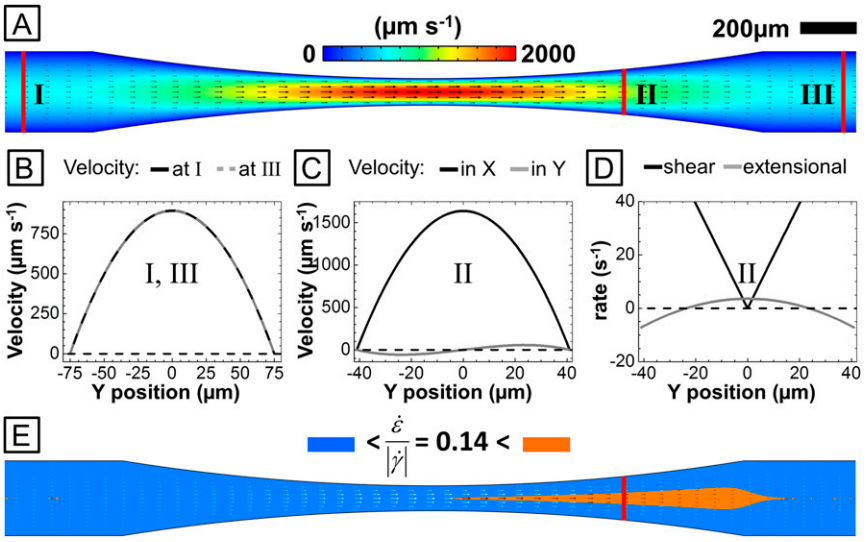

Fig. S3. (*A*) Calculated velocity field $\vec{v}(x,y)$ of water across the contraction/expansion region in the narrow channel section. (*B*) Calculated velocity profiles $v_x(y)$ in the pretapering zone I (solid black line) and posttapering zone III (dashed gray line). (*C*) Velocity profiles $v_x(y)$ (solid black line) and $v_y(y)$ (solid gray line) in the expansion zone indicated in red in *A*. (*D*) Shear rate $|\dot{\gamma}(y)|$ (solid black line) and extensional rate $\dot{\varepsilon}(y)$ (solid gray line) in the expansion zone. (*E*) Map of the ratio $\dot{\varepsilon}/|\dot{\gamma}|$ in the wide and narrow channel sections. In the orange regions, $\dot{\varepsilon}/|\dot{\gamma}| > 0.14$, whereas in the blue regions, $\dot{\varepsilon}/|\dot{\gamma}| < 0.14$.

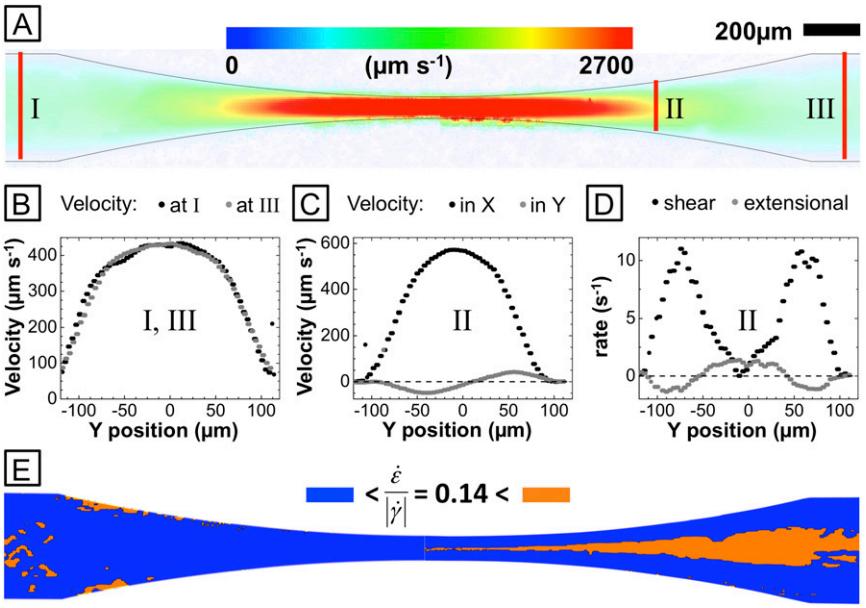

Fig. S4. Flow profiles $v_x(x,y)$, $v_y(x,y)$ of water measured by μPIV. (*A*) Modulus of the measured particle velocity in the wide and narrow channel sections. (*B*) Velocity profile $v_x(y)$ in the pretapering zone I (black circles) and posttapering zone III (gray circles). (*C*) Velocity profiles $v_x(y)$ (black circles) and $v_y(y)$(gray circles) in the expansion zone II. (*D*) Shear rate $\dot{\gamma}(y)$ (black circles) and extensional rate $\dot{\varepsilon}(y)$ (gray circles) in the expansion zone II. (*E*) Map of the ratio $\dot{\varepsilon}/|\dot{\gamma}|$ in the wide and narrow channel sections. In the orange regions, $\dot{\varepsilon}/|\dot{\gamma}| > 0.14$, whereas in the blue regions, $\dot{\varepsilon}/|\dot{\gamma}| < 0.14$. The resulting color map shows that even for pure water, there is a region with considerable perpendicular extensional forces in the expansion zone.

Fig. S5. Polarization microscopy reveals the flow behavior of polyethylenebutylene-*b*-ethylene oxide (PEB-PEO) micelles (30% wt/wt in water) in consecutive taperings. In this example, the micelles are pumped through a 250-μm channel with two 250-μm taperings at a rate of 300 μL/h. The flow orientation is from left to right. (Scale bar: 200 μm.)

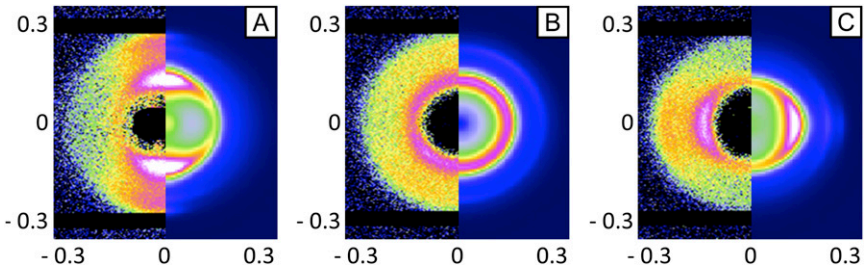

Fig. S6. Typical measured (*Left*) and simulated (*Right*) scattering patterns in the contraction zone (*A*), at the beginning of the expansion zone (*B*), and in the central part of the expansion zone (*C*) along the central flow line similar as in Fig. 2*C*.

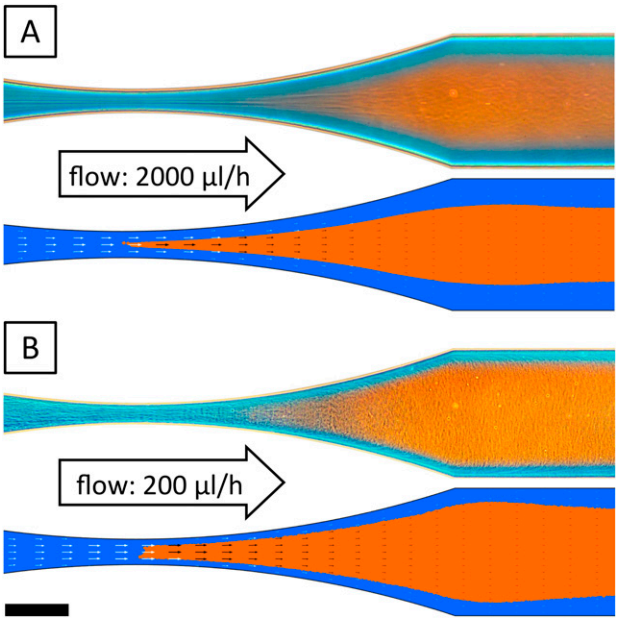

Fig. S7. Measured and simulated areas of high extensional flow and perpendicular alignment (orange zone). For high flow rates (*A*), the orange region is more confined to the central part of the channel in comparison to low flow rates (*B*).

Table S1. Material properties used in the simulation model

Fig. 5 and Fig. S3 (ref.)	Non-Newtonian	Newtonian
Flow rate, v_{flow}; $\mu L \cdot h^{-1}$	32.4	32.4
Flow speed, v; $mm \cdot s^{-1}$	18.52	18.52
Zero-shear viscosity, η_0; Pa/s	19,522	—
High-shear viscosity, η_∞; Pa/s	0.1	—
Internal relaxation time, τ_c; s	388.5	—
Power-law exponent	0.99	—
Viscosity, η; $kg \cdot m^{-1} \cdot s^{-1}$ (1)	—	$1.002 \cdot 10^{-3}$
Density, ρ; $kg \cdot m^{-3}$ (2)	998.2	998.2
Temperature, T; K	293.15	293.15

1. Weast R, Astle M (1979) *Handbook of Chemistry and Physics* (CRC, Boca Raton, FL), 60th Ed, p F-11, F-49.
2. (2011) *User's Guide for COMSOL Multiphysics v4.2a* (COMSOL AB), pp 612–627.

Table S2. Parameters for quantitative calculations in Fig. S6

Fig. 3	A	B	C
Cylinder length, L; nm	104	104	104
Relative SD, σ_L	0.13	0.13	0.13
Cylinder radius, R; nm	13.3	13.3	13.3
Relative SD, σ_R	0.13	0.13	0.13
Unit cell dimension, a; nm	58	58	58
Mean deviation, σ_a; nm	7.5	7.5	7.5
Mean deviation angle, δ; °	40	360	50
Radial domain size, D_l; nm	105	105	105
Azimuthal coherence length, D_ψ; nm	35	8	25